Numerical and Experimental Demonstration of Intermodal Dispersive Wave Generation

Niklas M. Lüpken, Maximilian Timmerkamp, Ramona Scheibinger, Kay Schaarschmidt, Markus A. Schmidt, Klaus-J. Boller, and Carsten Fallnich*

Evidence of intermodal dispersive wave generation mediated by intermodal cross-phase modulation (iXPM) between different transverse modes during supercontinuum generation in silicon nitride waveguides is presented. The formation of a higher-order soliton in one strong transverse mode leads to phase modulation of a second, weak transverse mode by iXPM. The phase modulation enables not only supercontinuum generation but also dispersive wave generation within the weak mode, that otherwise has insufficient power to facilitate dispersive wave formation. The nonlinear frequency conversion scheme presented here suggests phase-matching conditions beyond what is currently known, which can be exploited for extending the spectral bandwidth within supercontinuum generation.

1. Introduction

By providing light with an ultra-broad bandwidth at a high degree of coherence, supercontinua are of high interest for many applications, such as optical coherence tomography,[1] frequency comb generation,[2] frequency metrology,[3] or coherent Raman spectroscopy.[4] Supercontinuum generation (SCG) has been investigated numerically as well as experimentally in, for example, optical fibers,[5–8] photonic crystal fibers,[9–13] multi-material fibers,[14] liquid-core fibers,[15,16] and various integrated waveguides with different core materials.[17–24] One strategy for ultra-broad supercontinua involves higher-order soliton (HOS) fission in the anomalous dispersion regime associated with dispersive wave (DW) generation, phase-matched in the normal dispersion regime.[25] As of now, all schemes for DW generation are restricted to the case that all involved optical fields propagate in the same, single fundamental transverse mode.

In multi-mode nonlinear waveguides, also higher-order transverse modes can nonlinearly interact with each other, for instance via intermodal cross-phase modulation (iXPM) and intermodal four-wave mixing (iFWM).[26] While iXPM is solely a phase modulation between transverse modes, iFWM includes amplitude modulations, transferring energy between transverse modes. Many multi-mode interactions were already investigated numerically as well as experimentally, such as multi-mode SCG,[6,13] higher-order mode SCG,[16] multi-mode solitons,[5] iFWM,[27] all-optical switching,[28] intermodal third-harmonic generation,[23] geometric parametric instability,[29] soliton self-mode conversion,[30] and beam self-cleaning.[31] With the increased number of transverse modes in multi-mode waveguides, the complexity of the nonlinear dynamics increases but enables new phase-matching opportunities for frequency generation. Hence, multi-mode integrated waveguides have gained an increasing attention in the recent years, for example, for second-harmonic generation,[32,33] frequency comb generation in the visible,[23,34] quantum optics,[35] or all-optical switching.[28]

In this work, we present numerical as well as experimental evidence of a new mechanism for DW generation between different transverse modes, namely intermodal DW generation (iDWG). This process is mediated by iXPM, where HOS formation in one mode induces a DW in a different mode. In contrast to previous generation of DWs in a different transverse mode via iFWM,[13,36] the effect of iDWG is solely due to phase modulation and no energy is transferred between transverse modes. Earlier simulations of SCG in liquid-core fibers[16] may have contained traces of the new generation dynamics, however, this was neither investigated theoretically nor reported experimentally. Here, we report on experiments with accompanying numerical simulations proving the existence of iDWG and unraveling the underlying mechanism. We conclude that the iDWG has the potential to

N. M. Lüpken, M. Timmerkamp, Prof. K.-J. Boller, Prof. C. Fallnich
Institute of Applied Physics
University of Münster
Corrensstraße 2, 48149 Münster, Germany
E-mail: n.luepken@uni-muenster.de

R. Scheibinger, K. Schaarschmidt, Prof. M. A. Schmidt
Leibniz Institute of Photonic Technology
Albert-Einstein-Str. 9, 07745 Jena, Germany

Prof. M. A. Schmidt
Otto Schott Institute of Material Research
Friedrich Schiller University of Jena
Fraunhoferstr. 6, 07743 Jena, Germany

Prof. K.-J. Boller, Prof. C. Fallnich
MESA+ Institute for Nanotechnology
University of Twente
Enschede 7500 AE, The Netherlands

The ORCID identification number(s) for the author(s) of this article can be found under https://doi.org/10.1002/lpor.202100125

DOI: 10.1002/lpor.202100125

specifically increase the bandwidth during SCG or to generate radiation in hard-to-access frequency domains and modes.

As a model system for the verification of the existence of iDWG and its characterization, we used rectangular silicon nitride waveguides, featuring reliable and efficient SCG due to the high nonlinear refractive index coefficient and the tight modal confinement.[2,20,21,23,37–39] Due to waveguide birefringence, as also exploited for SCG in silicon,[37] the waveguides feature two fundamental transverse modes that are distinguishable by polarization (TE_{01} and TM_{01} mode), that is, they can be separated by means of a polarizer and variably excited by adjusting the input polarization. This waveguide system allows for single-mode measurements in direct comparison to straightforward multi-mode measurements by launching only one or both fundamental transverse modes, respectively.

2. Theoretical Investigation of Intermodal Dispersive Wave Generation

In order to analyze the effect of iDWG on the basis of a clear experiment, we consider two different transverse modes excited together, of which only one mode (the strong mode, here TE_{01}) has sufficient energy to form a HOS, and therewith is able to generate DWs during fission. The other mode (the weak mode, here TM_{01}) has insufficient energy to generate a DW. Under these circumstances one would intuitively expect that the strong mode induces some general spectral broadening of the weak mode, but no DW formation. Instead, we observe in simulations as well as in experiments that the weak mode generates its own DWs in spite of insufficient pulse energy for even forming a soliton.

In order to investigate the underlying mechanism of iDWG, we performed nonlinear pulse propagation simulations for a 1 μm wide and 0.9 μm high waveguide based on the nonlinear Schrödinger equation (for details see Supporting Information). The dispersion parameters of both modes are plotted as a function of the wavelength in Figure S1a,d, Supporting Information. First, only the TE_{01} mode was excited as the strong mode with a high input energy of 170 pJ, sufficient to generate a HOS and one DW in the infrared spectral domain. The corresponding spectral evolution as a function of the propagation distance is shown color-coded in **Figure 1**c. After spectral broadening due to self-phase modulation (SPM) a HOS formed, which generated a DW at approximately 2.2 μm wavelength after soliton fission due to the spectral overlap with the DW. The white dashed line highlights the DW wavelength calculated from the phase mismatch (plotted in Figure 1a, see Equation (S2), Supporting Information), showing a good agreement with the simulation. Second, the TM_{01} mode was excited as the weak mode in the absence of the strong mode with a much lower input energy of about 20 pJ. The launched pulse energy was insufficient to enable the formation of a soliton and, therefore, no spectral broadening and no DW formation appeared (see spectral evolution in Figure 1d).

To reveal the existence and novel nature of iDWG, both modes were excited simultaneously with energies of 170 and 20 pJ for the TE_{01} mode and the TM_{01} mode, respectively. In this case, the strong TE_{01} mode, shown in Figure 1e, generated a supercontinuum and a DW, resembling the single-mode case, because iXPM induced by the weak TM_{01} mode was negligible. The important difference with single-mode excitation is found in the weak mode (see Figure 1f): the strong mode induces noticeable spectral broadening of the weak mode by iXPM, comparable in width to the strong mode. Thereby, the spectrum of the weak mode becomes sufficiently broad to spectrally overlap with the phase-matched wavelength of a DW, causing the formation of a DW, while the weak mode with a soliton number of 0.97 is not able to generate a DW on its own in absence of the strong mode (compare with Figure 1d). Note that the pulse energy in the weak mode remains the same at any propagation distance, that is, a part of the energy is only shifted from the center frequency of the weak mode into a corresponding DW, without an exchange of energy between both modes. For improved visualization of the iDWG process an animated video including the temporal and spectral amplitudes can be found in the Supporting Information.

In order to numerically validate the mechanism of iDWG, the impact of different nonlinear effects within iDWG was investigated by performing numerical simulations where individual nonlinear contributions and effects were selectively disabled. First, the effect of iXPM was disabled by setting the nonlinear coupling coefficients $Q_{2211} = Q_{2121} = 0$, while leaving the coupling coefficients for iFWM and SPM unchanged (see Equation (S1), Supporting Information). The corresponding spectral evolution of the strong mode (shown in Figure 1g) showed no significant changes compared to the case of enabled iXPM. The spectral evolution of the weak mode (Figure 1h), however, showed no DW formation due to the negligible SPM-induced spectral broadening. Second, we performed simulations in which iFWM was disabled (i.e., $Q_{1222} = Q_{2111} = 0$), nevertheless showing generation of a DW in the weak mode if iXPM was enabled. This proves that iDWG does not rely on energy exchange between the modes but solely on phase modulation. Lastly, numerical simulations, in which SPM of the strong mode was disabled ($Q_{1111} = 0$) preventing HOS formation in the strong mode, did not show spectral broadening or the generation of a DW in the weak mode, hence, the formation of a HOS in the strong mode is necessary in order to achieve a sufficiently short and intense pulse, that is, a high peak power, for a highly effective cross-phase modulation. Therefore, we conclude that the iXPM-mediated interaction between the strong TE_{01} and the weak TM_{01} mode is the central mechanism that generates intermodal DWs.

In order to derive a phase-matching condition for iDWG based on the above described nonlinear dynamics, the phase of both the dispersive wave (at angular frequency ω_d) and the pulse (at angular frequency ω_p) in the weak mode have to be evaluated in the reference frame of the soliton (at angular frequency ω_s) propagating in the strong mode. These conditions imply that the propagation constants of the weak mode $\beta^{(weak)}(\omega)$ as well as of the strong mode $\beta^{(strong)}(\omega)$ have to be considered for the phase-matching condition

$$\beta^{(weak)}(\omega_d) - \beta_1^{(strong)}(\omega_s)\omega_d = \beta^{(weak)}(\omega_p) - \beta_1^{(strong)}(\omega_s)\omega_p + \gamma_{XPM} P_s \tag{1}$$

where $\beta_1^{(strong)}(\omega_s)$ is the inverse group velocity of the soliton in the strong mode, γ_{XPM} the nonlinear coefficient of iXPM, and P_s the peak power of the soliton in the strong mode.

In general, ω_p and ω_s can differ, but in our case, as the pulses in the weak and strong mode have the same center frequency, the angular frequency of the weak mode coincides with the angular

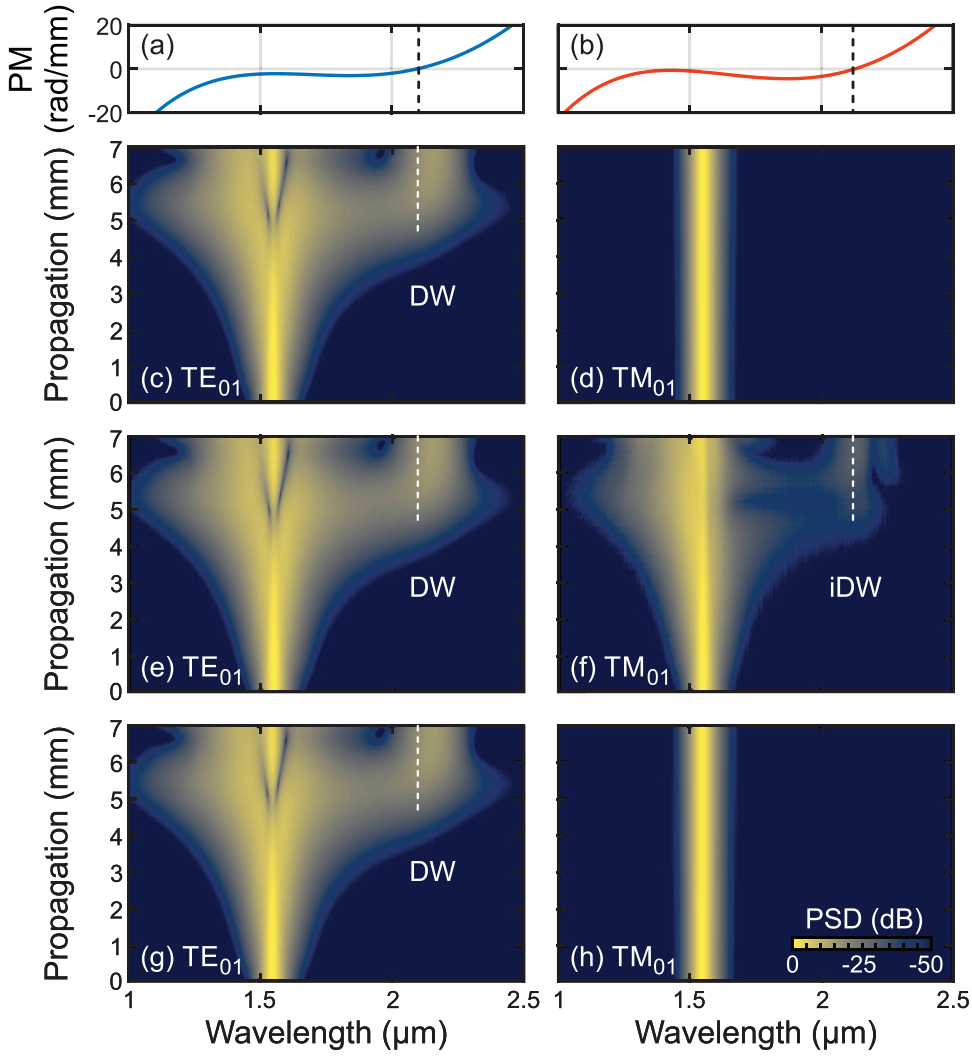

Figure 1. Comparison of single-mode and multi-mode simulations demonstrating the effect of intermodal dispersive wave generation. Phase mismatch (PM) as a function of the wavelength for a) the single-mode case and b) the multi-mode case. Single-mode simulations of the normalized spectral evolution of c) a strong TE_{01} mode and d) a weak TM_{01} mode. Spectral evolution of e) the strong TE_{01} mode and f) the weak TM_{01} mode in a simulation with both modes excited simultaneously. g,h) Same simulations as in e) and f) but with disabled iXPM. The launched energy of the TE_{01} and TM_{01} modes correspond to 170 and 20 pJ in all simulations, respectively. The white dashed lines correspond to the phase-matched wavelengths. To demonstrate the effect in more detail, an animated video including the temporal and spectral amplitudes can be found in the Supporting Information.

frequency of the soliton $\omega_p = \omega_s$. Then, expanding the propagation constants in a Taylor series leads to the multi-mode phase mismatch

$$\Delta k_{MM} = \sum_{m=2}^{\infty} \frac{\beta_m^{(weak)}(\omega_s)}{m!} (\omega_d - \omega_s)^m - \Delta\beta_1 \cdot (\omega_d - \omega_s) - \gamma_{XPM} P_s \tag{2}$$

where $\beta_m^{(weak)}$ is the m-th dispersion coefficient of the weak mode and $\Delta\beta_1 = \beta_1^{(strong)}(\omega_s) - \beta_1^{(weak)}(\omega_s)$ the group velocity mismatch between the pulse in the weak mode and the soliton in the strong mode. The phase-matched wavelength for an intermodal DW in the weak mode ($\Delta k_{MM} = 0$), calculated from the phase mismatch plotted in Figure 1b, matches the wavelength of the simulated intermodal DW (see dashed white line in Figure 1f). In contrast to the single-mode phase-matching condition (see Equation (S2), Supporting Information), the multi-mode phase-matching condition additionally includes the group velocity mismatch of the participating modes. By artificially changing the relative group velocities in additional numerical simulations and comparing the according wavelengths of the iDWs with the calculated phase-matched wavelengths, we verified the impact of the group velocity mismatch on the phase-matched wavelength and validated the derived phase-matching condition for iDWG. However, a detailed investigation of the impact of the relative group velocities is out of the scope of this work and will be the target of future investigations. Nevertheless, the good agreement between the wavelength of the iDW and the phase-matching calculations (see Figure 1f) validates that iXPM between the soliton in the strong mode and the pulse in the weak mode, as described above, is the central mechanism for iDWG.

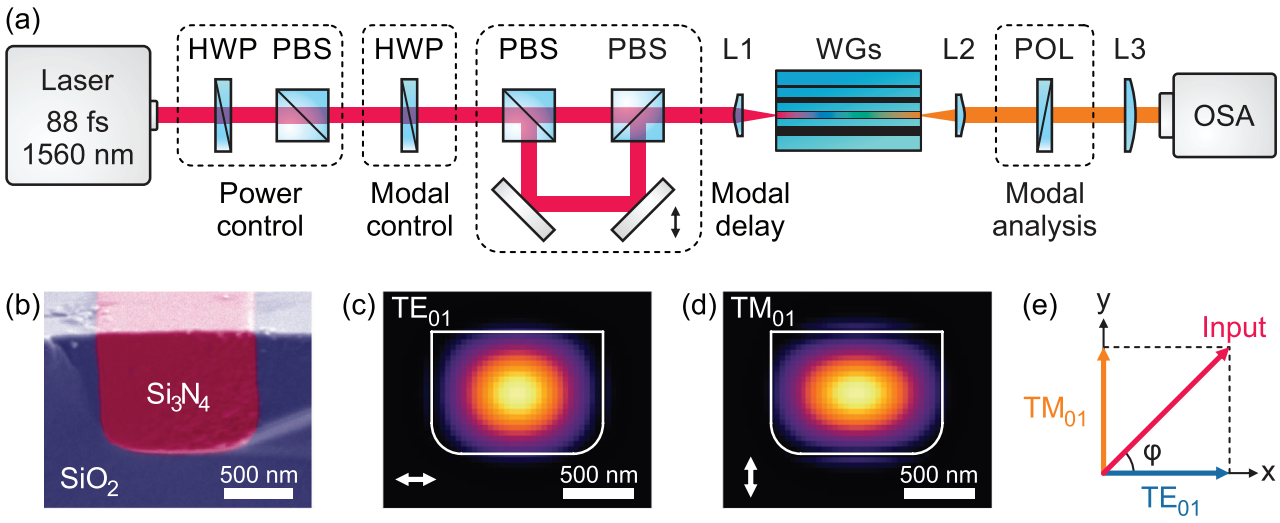

Figure 2. a) Schematic of the experimental setup. HWP:, half-wave plate; PBS, polarizing beam splitter; L, aspherical lens; WGs, silicon nitride waveguides; POL, polarizer; OSA, optical spectrum analyzer. See text for details. b) SEM image of a 0.9 µm high and 1.2 µm wide silicon nitride (Si_3N_4) waveguide embedded in silica (SiO_2, without top cladding). Calculated mode profiles of c) TE_{01} and d) TM_{01} modes. The arrows in the bottom left corner depict the polarization axis. e) Schematic of the modal power control by adjusting the direction of the input polarization via the second HWP.

3. Experimental Section

In order to experimentally verify the existence of iDWG, we realized a setup enabling the full control over the amplitudes of both orthogonal modes and their relative delay. We used two waveguides with widths of 1.0 and 1.2 µm for DW generation in the infrared and visible spectral domains, respectively. The 1.0 µm wide waveguide was selected because it would allow to generate a DW in the weak mode without using a relative delay due to a sufficiently low modal walk-off (70 fs at the end of the waveguide, smaller than the pulse duration), enabling a simplified experimental setup without a delay line. However, this waveguide exhibited multiple spectral features at visible wavelengths (see Figure S2, Supporting Information), for example, due to intermodal third-harmonic generation (iTHG), which inhibited the clear observation of the weak DW. The other 1.2 µm wide waveguide was used due to the absence of such ambiguous spectral features, although compensation of modal walk-off (250 fs at the end of the waveguide, equal to 2.8 times the pulse duration) with a delay stage was required. With this waveguide, iDWG was clearly observable in the visible due to the absence of other spectral contributions.

3.1. Setup

The experimental setup allows control over the power in each mode and the temporal delay between both modes. A schematic of the experimental setup is shown in **Figure 2**a: Pulses from an ultra-fast fiber laser centered at 1560 nm wavelength with a pulse duration of 88 fs at a repetition rate of 80 MHz were used. The optical power, coupled into the silicon nitride waveguide with an aspherical lens, was controlled with a combination of a half-wave plate (HWP) and a polarizing beam splitter (PBS). The available silicon nitride waveguides were 7 mm long, 0.9 µm high, and their widths ranged from 0.8 to 1.3 µm. An exemplary SEM image of a 1.2 µm wide waveguide is shown in Figure 2b, whose rounded bottom edges were taken into account when the mode profiles of the TE_{01} mode and TM_{01} mode (Figure 2c,d) were calculated with a mode solver (finite differences mode solver from Photon Design). Note that the SEM image was acquired before the silica top-cladding was added to the used waveguides. The input power P_0 was divided between both modes by adjusting the angle φ of the input polarization (compare Figure 2e) via a second half-wave plate, such that the powers of the excited TE_{01} and TM_{01} modes correspond to $P_{TE} = P_0\,\eta_{TE}\,\cos^2(\varphi)$ and $P_{TM} = P_0\,\eta_{TM}\,\sin^2(\varphi)$, respectively, with the mode-specific coupling efficiencies η. Theoretically, the coupling efficiencies should differ slightly due to the different mode profiles; however, within the uncertainty margin of the experiments, a coupling efficiency of $\eta_{TE} = \eta_{TM} = 35\,\%$ was estimated from transmission measurements. In the following, the denoted powers and pulse energies refer to the waveguide-internal values. A following unbalanced Mach-Zehnder interferometer allowed control on the modal delay. To concentrate on the principal functionality of the setup some components of the interferometer are not shown in Figure 2a: a telescope was placed into the longer interferometer arm to compensate the beam divergence, and additional polarizers were placed into each arm in front of the combining PBS to improve the limited extinction ratio of the available polarizing optics. The waveguide output was collimated with a second lens and the mode of interest was selected with a polarizer (up to 34 dB polarization contrast) such that the output of each mode could be individually measured with an optical spectrum analyzer (Ando AQ-1425, 400–1600 nm, or Yokogawa AQ6376, 1500–3400 nm).

3.2. Generation of Intermodal Dispersive Waves in the Infrared Spectral Domain

In order to measure iDWG in the infrared spectral domain with the 1.0 µm wide waveguide, the strong TE_{01} mode and the weak TM_{01} mode were simultaneously excited with pulse energies of

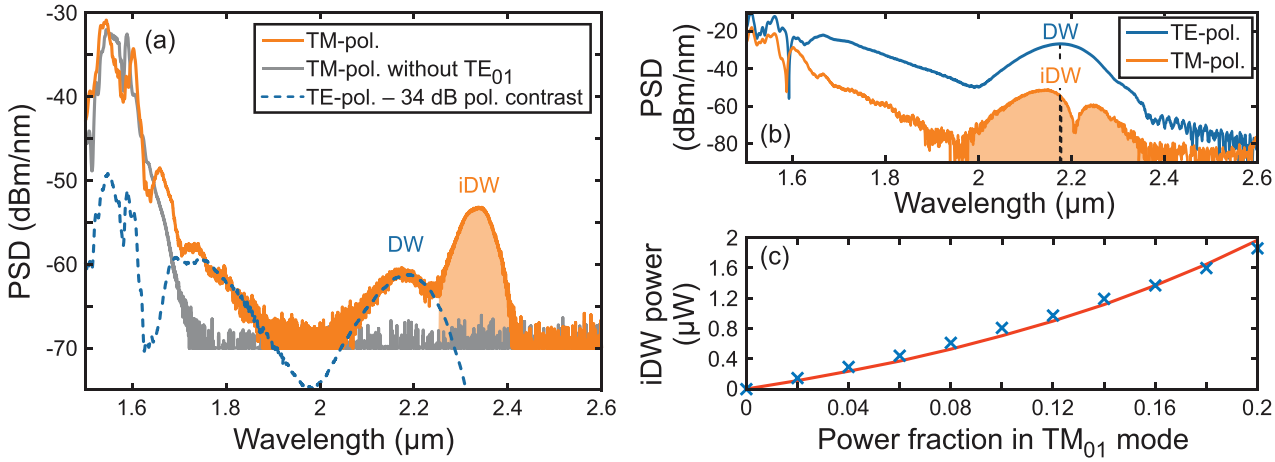

Figure 3. a) Output power spectral density (PSD) when only the TE_{01} mode (blue), only the TM_{01} mode (gray), and both modes detecting the TM-polarization (orange) are excited in the 1.0 μm wide silicon nitride waveguide. b) Corresponding simulated output spectra of the TE_{01} mode (blue) and the TM_{01} mode (orange) when both modes were excited simultaneously. The dashed lines mark the phase-matched wavelengths of the DW and the iDW. c) Power of the TM-polarized intermodal DW (iDW) as a function of the power fraction coupled into the TM_{01} mode for measurement (blue crosses) and simulation (red line). For details see text.

about 200 and 50 pJ, respectively. At these input energies, the strong mode generated a single DW in the infrared spectral domain and the weak mode generated no DW on its own, which was verified by measuring the output spectrum of the weak mode if it was solely excited in the waveguide (gray curve in **Figure 3**a). When both modes were excited simultaneously and solely the TM-polarization was detected (orange curve in Figure 3a), spectral broadening of the strong mode was observable and two peaks became visible at 2.2 and 2.35 μm wavelength. The measurement of the spectrum of the strong TE_{01} mode (blue curve in Figure 3a), reduced by the polarization contrast of up to 34 dB to exclude cross-talk due to the limited contrast of the polarizer for modal analysis, revealed that the signals at 1.8 and 2.2 μm originated from spectral broadening and DW generation in the strong mode, respectively. However, the signal at 2.35 μm (orange-shaded area) clearly showed an iDW, generated by iXPM-mediated interaction between both modes, because it was not observed for the strong TE_{01} mode, thus confirming the observation of iDWG. While a record bandwidth of 537 THz was measured in the single-mode case (see Supporting Information), the iDW extended the spectral bandwidth by about 150 nm.

In addition to the experiment, numerical simulations verified the iDWG (see Figure 3b) and showed good agreement with the experimental data. The strong TE_{01} mode generated a DW at 2.2 μm wavelength while an iDW was generated in the weak TM_{01} mode at 2.15 μm wavelength. These wavelengths coincide with the phase-matched wavelengths plotted as dashed lines, which were predicted by the phase mismatch (see Equation (2) and Equation (S2), Supporting Information). When no power was launched into the strong mode, no DW was generated by the weak mode. The modulation of the DW around 2.2 μm wavelength in the weak mode originated from spectral interference of two DWs (see Supporting Information) in the weak mode. The wavelength of the iDW in the simulation differed from the wavelength measured in the experiments, which will be discussed in Section 3.4.

In order to investigate the dependence of iDWG on the power fraction of the TM_{01} mode, measurements with increasing power launched into the TM_{01} mode were performed, while the pulse energy of the excited TE_{01} mode was fixed at 200 pJ for all measurements with the appropriate control of both half-wave plates (see Figure 2a). With increasing input power in the weak mode the generated iDW power (blue crosses in Figure 3c) increased, matching well with the simulated iDW power (red line in Figure 3c). Note that the weak mode reached a soliton order of 1.6 at a power fraction of 0.2, however, corresponding to a fission length of 12 mm, that is, 5 mm longer than the waveguide length.

3.3. Generation of Intermodal Dispersive Waves in The Visible Spectral Domain

For iDWG in the visible spectral domain, a 1.2 μm wide waveguide was used as it exhibited no iTHG signals that spectrally overlapped with the DW (compare Supporting Information). However, due to a larger modal walk-off the delay stage had to be used to improve the temporal overlap of the strong and weak modes during fission. **Figure 4**a shows the experimental spectra measured when the strong TE_{01} mode and the weak TM_{01} mode were excited with pulse energies of 350 and 40 pJ, respectively, and delayed with respect to each other, such that the DW power of the weak mode was maximized. The higher input power in the strong mode was required to generate a DW in the visible spectral domain (compare Figure S1, Supporting Information). The spectrum of the strong mode was corrected by subtracting the polarization contrast (up to 25 dB) to exclude TE-polarized signals in the TM-polarized spectrum, occurring due to the limited polarization contrast of the modal analysis. When the weak mode was solely excited with a pulse energy of 40 pJ, the output spectrum showed no DW (see gray curve in Figure 4a), because the weak mode had a soliton order of unity with a corresponding fission length of 12 mm, significantly exceeding the waveguide length.

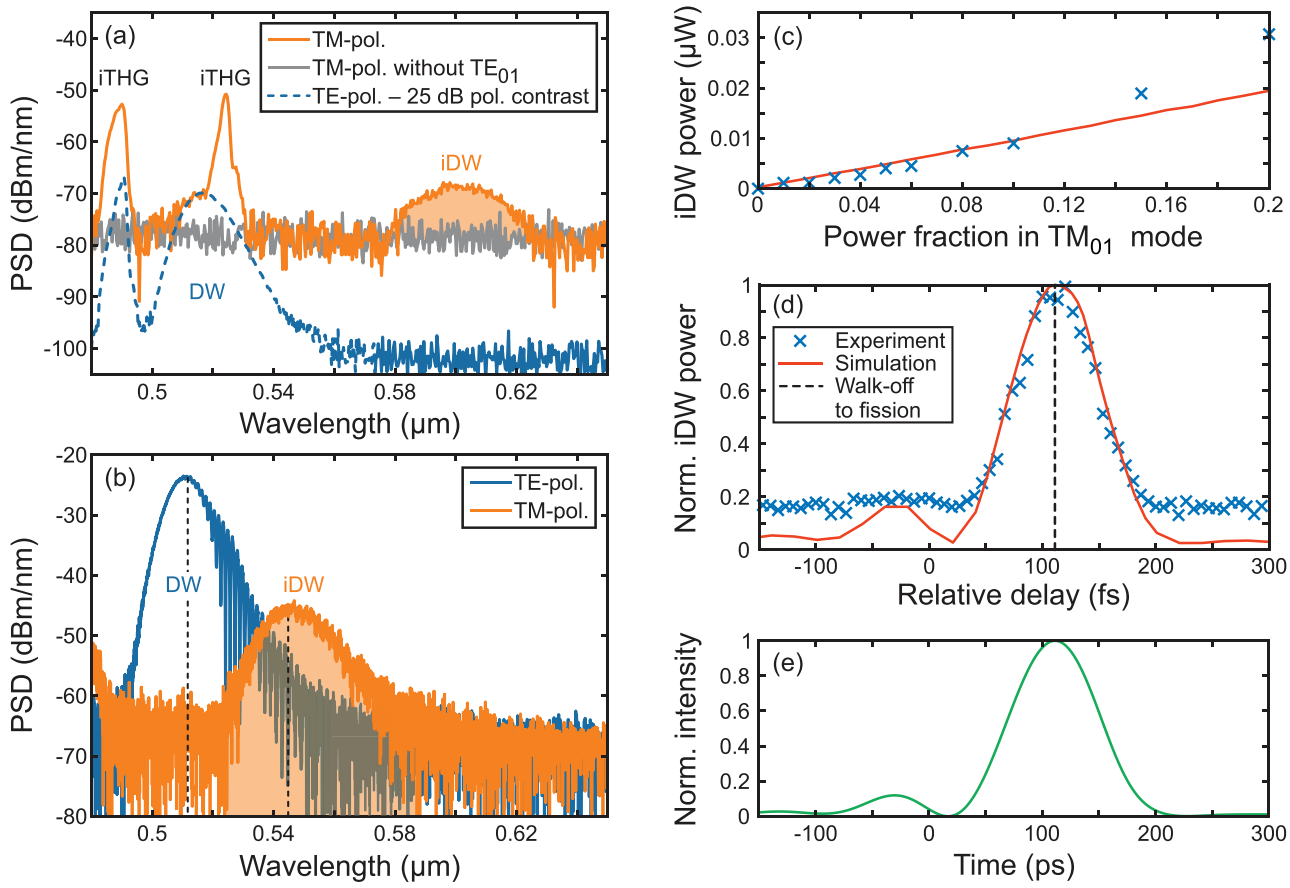

Figure 4. a) Output spectra when only the TE_{01} mode (blue), only the TM_{01} mode (gray), and both modes (detecting only the TM-polarization, orange curve) were excited in the silicon nitride waveguide (1.2 μm width), where iTHG and iDW denote third-harmonic signals and DWs generated by iDWG, respectively. b) Corresponding simulated output spectra of the TE_{01} mode (blue) and the TM_{01} mode (orange), when both modes were excited. The dashed lines mark the phase-matched wavelengths of the DW and the iDW. c) Measured (blue crosses) and simulated (red line) power of the iDW in the weak mode as a function of the TM_{01} mode's input power fraction. d) Measured (blue crosses) and simulated (red line) normalized iDW power as a function of the relative delay between the pulses in each mode. The black vertical dashed line indicates the accumulated temporal walk-off at the fission point. e) Temporal pulse shape of the input pulses retrieved from FROG measurements.

When both modes were excited simultaneously, different spectral features appeared in the visible wavelength domain of the TM_{01} mode spectrum (orange curve in Figure 4a): the narrowband signals around 500 nm corresponded to iTHG signals generated from the TE_{01} mode in higher-order transverse modes (see Figure S2, Supporting Information), as these hybrid modes have contributions in both orthogonal polarization directions. The iTHG signals were identified by measuring the mode profiles, showing higher-order modes, and examining the phase-matching condition. Due to contributions in both polarizations, these signals were even visible when no power was launched into the weak mode. As cross-talk of the TE_{01} mode only occurred at wavelengths below 530 nm (see blue curve in Figure 4a), the broad peak around 600 nm (orange shaded area) corresponded unambiguously to a DW in the TM_{01} mode generated by iDWG.

Corresponding numerical simulations with the experimental pulse and waveguide parameters verified the appearance of iDWG (see Figure 4b): When the power of the strong mode was set to zero in the simulations, no DW was generated in the weak mode. When both modes were excited simultaneously, the strong mode generated a DW at 510 nm wavelength while an iDW was generated in the weak mode at 550 nm wavelength, which coincide with the phase-matched wavelengths (see dashed lines in Figure 4b) predicted by the phase mismatch (see Equation (2) and Equation (S2), Supporting Information). The modulations on the long-wavelength side of the weak and strong modes' DW spectra originated from spectral interference of two DWs (see Supporting Information).

The power dependence of the iDW on the power fraction of the weak TM_{01} mode (blue crosses) is shown in Figure 4c, when the strong TE_{01} mode was excited with a fixed pulse energy of 350 pJ. With increasing pulse energy in the weak mode the power of the generated iDW increased, in accordance with the simulated iDW power (red line in Figure 4c). However, for power fractions larger than 0.14, the measured iDW power deviated from the simulated values, which will be discussed in Section 3.4.

In order to investigate in detail the mechanism of iDWG and how temporal walk-off between the involved transverse modes reduces the efficiency of the iDWG, output spectra with different relative delays between the pulses of the excited transverse

modes were acquired. The normalized power of the generated iDW in the weak TM_{01} mode is depicted in Figure 4d as a function of the relative delay between the TE_{01} and TM_{01} mode for the experiment (blue crosses) and the simulation (red line). The delay axis was adjusted to match its zero with the maximal DW power in the simulations as no temporal reference was available in the experiments. The simulated data matched the experimental data, however, the signal-to-noise ratio was lower in the experiments, leading to a background signal of approximately 0.18. The peak at −25 fs in the simulations originated from a preceding satellite pulse visible in the temporal pulse shape (compare Figure 4e) retrieved from FROG measurements. Furthermore, the maximum DW power was reached for a delay of 116 fs, which agreed well with the accumulated modal walk-off (36 fs mm^{-1}) to the fission point at 3.1 mm propagation length (marked as a dashed line in Figure 4d). Note that the obtained DW power curve corresponds to a cross-correlation of the input pulse in the weak mode and the HOS at the fission point. Within the measurement uncertainties, the temporal width of 94 fs matched the full width at half maximum of a calculated cross-correlation (91 fs) between the input pulse (88 fs) and the HOS (14 fs). The correspondence between the maximum of the iDW power with the expected temporal walk-off in conjunction with the fitting cross-correlation underlines that the origin of the iDW is related to iXPM between the weak mode and the HOS formed in the strong mode.

3.4. Discussion

The experimental and numerical data unambiguously prove the generation of iDWs and that the iXPM-mediated interaction of the HOS in the strong mode with the weak mode is the origin of this effect. Other spectral features such as iTHG signals and ordinary DWs could be excluded by the comparison with the single-mode case, and the delay-dependent generation of iDWs clearly confirmed that the interaction with the HOS is necessary for iDWG.

The comparison of the simulated and measured iDWG signals in the infrared and visible spectral domain revealed deviations in the wavelength and the measured power of the iDWs in the visible. As expected from the phase mismatch (see Equation (2)), differences of the relative group velocities of the participating modes had an influence on the wavelength and output power of the generated iDW in the two-mode case, which was verified by varying the group velocity $1/\beta_1$ of the weak mode in additional numerical simulations.

The influence of the relative group velocities makes the center wavelength and output power of the generated iDW more sensitive to changes of the dispersion profile. Therefore, the differences in wavelength of the iDWs between experiment and simulation can be explained by small deviations from the nominal waveguide height and width as well as uncertainties in the refractive index model. Especially the measured higher output powers of the iDW in the visible spectral domain (see Figure 4c) resulted from an additional energy contribution of ordinary DW formation, as the weak mode had sufficient energy to form a fundamental soliton (soliton order $N > 1.4$) within the weak mode for a power fraction above 0.12. This soliton within the weak mode radiated an additional DW, whose wavelength coincided with that of the iDW, while in simulations the iDW was radiated at a different wavelength on account of different group velocities. Nevertheless, good agreement between simulation and experiment of the power fraction scans (Figures 3c and 4c) and the delay scan (Figure 4d) was achieved, clearly proving the existence and impact of iDWG.

The increased sensitivity of the iDW wavelength location to the dispersion profile can be exploited to tune the output wavelength. First numerical simulations showed that changing the center wavelengths of the involved modes or altering the waveguide dispersion via engineering of the waveguide cross-section, changes the wavelength of the iDW on account of the different relative group velocities. Correspondingly, the dispersion could be engineered to increase the extended bandwidth into the infrared (see Figure 3a) or the visible spectral domain. Furthermore, the same holds when using different transverse modes, for example, higher-order transverse modes, due to the different dispersion profiles of the higher-order modes. Moreover, the dispersive waves could be tailored to enable self-referencing[40] or to access hard-to-reach spectral domains.

4. Conclusion

We discovered and investigated the mechanism of intermodal dispersive wave generation between a strong and a weak transverse mode in waveguides. The underlying physics was studied within simulations by switching various nonlinear effects on and off, revealing that intermodal cross-phase modulation was unambiguously responsible for the generation of the dispersive wave in the weak transverse mode, which in absence of the strong mode would not be able to generate a dispersive wave. According to the agreement between the numerical and experimental data with the derived phase-matching condition intermodal dispersive wave generation was verified as the mechanism for the origin of the observed dispersive waves.

The process of intermodal dispersive wave generation was experimentally demonstrated within supercontinuum generation in high-confinement silicon nitride waveguides, in conjunction with numerical modeling on the basis of the generalized nonlinear Schrödinger equation, matching the experimental observations. While a record bandwidth of 537 THz was measured in the single-mode case, in the two-mode case intermodal dispersive wave generation, reaching 600 nm and 2.35 μm wavelength, was found to extend the spectral coverage of supercontinuum generation by 150 nm into the infrared spectral domain.

First numerical simulations showed that using different center wavelengths or different (i.e., higher-order) transverse modes could drastically change the wavelengths of the intermodal dispersive waves in future experiments, suggesting a novel pathway for tailoring nonlinear frequency conversion. Therewith, it can be expected that intermodal dispersive wave generation can be exploited to increase the bandwidth of supercontinua, for example, for mid-infrared spectroscopy,[41] to enable self-referencing,[40] or to access spectral domains that are otherwise hard to reach.

Supporting Information

Supporting Information is available from the Wiley Online Library or from the author.

Acknowledgements

N.M.L. and M.T. contributed equally to this work. The authors thank Jörn P. Epping and LioniX International B.V. for support and fabrication of the silicon nitride waveguides. M.S. and R.S. acknowledge suppport from the Deutsche Forschungsgemeinschaft (DFG, German Research Foundation) via the grants SCHM2655/12-1 and 259607349/GRK2101, respectively.

Open access funding enabled and organized by Projekt DEAL.

Conflict of Interest

The authors declare no conflict of interest.

Data Availability Statement

The data that support the findings of this study are available from the corresponding author upon reasonable request.

Keywords

dispersive wave, nonlinear optics, silicon nitride, supercontinuum generation, transverse modes

Received: March 4, 2021
Revised: May 5, 2021
Published online: July 7, 2021

[1] G. Humbert, W. Wadsworth, S. Leon-Saval, J. Knight, T. Birks, P. St. J. Russell, M. Lederer, D. Kopf, K. Wiesauer, E. Breuer, D. Stifter, *Opt. Express* **2006**, *14*, 1596.
[2] V. Brasch, M. Geiselmann, T. Herr, G. Lihachev, M. H. P. Pfeiffer, M. L. Gorodetsky, T. J. Kippenberg, *Science* **2016**, *351*, 357.
[3] J. T. Woodward, A. W. Smith, C. A. Jenkins, C. Lin, S. W. Brown, K. R. Lykke, *Metrologia* **2009**, *46*, S277.
[4] H. Kano, H.-o. Hamaguchi, *Opt. Lett.* **2003**, *28*, 2360.
[5] L. G. Wright, W. H. Renninger, D. N. Christodoulides, F. W. Wise, *Opt. Express* **2015**, *23*, 3492.
[6] G. Lopez-Galmiche, Z. Sanjabi Eznaveh, M. A. Eftekhar, J. A. Lopez, L. G. Wright, F. Wise, D. Christodoulides, R. A. Correa, *Opt. Lett.* **2016**, *41*, 2553.
[7] H. Zia, N. M. Lüpken, T. Hellwig, C. Fallnich, K. Boller, *Laser Photon. Rev.* **2020**, *14*, 2000031.
[8] N. M. Lüpken, C. Fallnich, *Appl. Phys. B* **2020**, *126*, 183.
[9] J. Herrmann, U. Griebner, N. Zhavoronkov, A. Husakou, D. Nickel, J. C. Knight, W. J. Wadsworth, P. S. J. Russell, G. Korn, *Phys. Rev. Lett.* **2002**, *88*, 173901.
[10] G. Genty, M. Lehtonen, H. Ludvigsen, *Opt. Express* **2004**, *12*, 4614.
[11] T. Schreiber, T. V. Andersen, D. Schimpf, J. Limpert, A. Tünnermann, *Opt. Express* **2005**, *13*, 9556.
[12] J. M. Dudley, G. Genty, S. Coen, *Rev. Mod. Phys.* **2006**, *78*, 1135.
[13] F. Poletti, P. Horak, *Opt. Express* **2009**, *17*, 6134.
[14] N. Granzow, M. A. Schmidt, W. Chang, L. Wang, Q. Coulombier, J. Troles, P. Toupin, I. Hartl, K. F. Lee, M. E. Fermann, L. Wondraczek, P. S. Russell, *Opt. Express* **2013**, *21*, 10969.
[15] M. Chemnitz, M. Gebhardt, C. Gaida, F. Stutzki, J. Kobelke, J. Limpert, A. Tünnermann, M. A. Schmidt, *Nat. Commun.* **2017**, *8*, 42.
[16] R. Scheibinger, N. M. Lüpken, M. Chemnitz, K. Schaarschmidt, J. Kobelke, C. Fallnich, M. A. Schmidt, *Sci. Rep.* **2021**, *11*, 5270.
[17] C. R. Phillips, C. Langrock, J. S. Pelc, M. M. Fejer, J. Jiang, M. E. Fermann, I. Hartl, *Opt. Lett.* **2011**, *36*, 3912.
[18] Y. Yu, X. Gai, P. Ma, D. .Y. Choi, Z. Yang, R. Wang, S. Debbarma, S. J. Madden, B. Luther-Davies, *Laser Photon. Rev.* **2014**, *8*, 792.
[19] B. J. Hausmann, I. Bulu, V. Venkataraman, P. Deotare, M. Loncar, *Nat. Photonics* **2014**, *8*, 369.
[20] J. P. Epping, T. Hellwig, M. Hoekman, R. Mateman, A. Leinse, R. G. Heideman, A. van Rees, P. J. van der Slot, C. J. Lee, C. Fallnich, K.-J. Boller, *Opt. Express* **2015**, *23*, 19596.
[21] M. A. G. Porcel, F. Schepers, J. P. Epping, T. Hellwig, M. Hoekman, R. G. Heideman, P. J. M. van der Slot, C. J. Lee, R. Schmidt, R. Bratschitsch, C. Fallnich, K.-J. Boller, *Opt. Express* **2017**, *25*, 1542.
[22] N. Singh, M. Xin, D. Vermeulen, K. Shtyrkova, N. Li, P. T. Callahan, E. S. Magden, A. Ruocco, N. Fahrenkopf, C. Baiocco, B. P. P. Kuo, S. Radic, E. Ippen, F. X. Kärtner, M. R. Watts, *Light Sci. Appl.* **2018**, *7*, 17131.
[23] E. Obrzud, V. Brasch, T. Voumard, A. Stroganov, M. Geiselmann, F. Wildi, F. Pepe, S. Lecomte, T. Herr, *Opt. Lett.* **2019**, *44*, 5290.
[24] K. F. Lamee, D. R. Carlson, Z. L. Newman, S.-P. Yu, S. B. Papp, *Opt. Lett.* **2020**, *45*, 4192.
[25] S. Roy, S. K. Bhadra, G. P. Agrawal, *Curr. Sci.* **2011**, *100*, 321.
[26] F. Poletti, P. Horak, *J. Opt. Soc. Am. B* **2008**, *25*, 1645.
[27] J. Demas, P. Steinvurzel, B. Tai, L. Rishøj, Y. Chen, S. Ramachandran, *Optica* **2015**, *2*, 14.
[28] N. M. Lüpken, T. Hellwig, M. Schnack, J. P. Epping, K.-J. Boller, C. Fallnich, *Opt. Lett.* **2018**, *43*, 1631.
[29] L. G. Wright, S. Wabnitz, D. N. Christodoulides, F. W. Wise, *Phys. Rev. Lett.* **2015**, *115*, 223902.
[30] L. Rishøj, B. Tai, P. Kristensen, S. Ramachandran, *Optica* **2019**, *6*, 304.
[31] K. Krupa, A. Tonello, B. M. Shalaby, M. Fabert, A. Barthélémy, G. Millot, S. Wabnitz, V. Couderc, *Nat. Photonics* **2017**, *11*, 237.
[32] J. S. Levy, M. A. Foster, A. L. Gaeta, M. Lipson, *Opt. Express* **2011**, *19*, 11415.
[33] M. A. G. Porcel, J. Mak, C. Taballione, V. K. Schermerhorn, J. P. Epping, P. J. M. van der Slot, K.-J. Boller, *Opt. Express* **2017**, *25*, 33143.
[34] L. Wang, L. Chang, N. Volet, M. H. P. Pfeiffer, M. Zervas, H. Guo, T. J. Kippenberg, J. E. Bowers, *Laser Photon. Rev.* **2016**, *10*, 631.
[35] A. Mohanty, M. Zhang, A. Dutt, S. Ramelow, P. Nussenzveig, M. Lipson, *Nat. Commun.* **2017**, *8*, 14010.
[36] J. Cheng, M. E. V. Pedersen, K. Charan, K. Wang, C. Xu, L. Grüner-Nielsen, D. Jakobsen, *Opt. Lett.* **2012**, *37*, 4410.
[37] N. Singh, D. Vermulen, A. Ruocco, N. Li, E. Ippen, F. X. Kärtner, M. R. Watts, *Opt. Express* **2019**, *27*, 31698.
[38] N. M. Lüpken, T. Würthwein, J. P. Epping, K.-J. Boller, C. Fallnich, *Opt. Lett.* **2020**, *45*, 3873.
[39] N. M. Lüpken, T. Würthwein, K.-J. Boller, C. Fallnich, *Opt. Express* **2021**, *29*, 10424.
[40] A. S. Mayer, A. Klenner, A. R. Johnson, K. Luke, M. R. E. Lamont, Y. Okawachi, M. Lipson, A. L. Gaeta, U. Keller, *Opt. Express* **2015**, *23*, 15440.
[41] D. Grassani, E. Tagkoudi, H. Guo, C. Herkommer, F. Yang, T. J. Kippenberg, C. S. Brès, *Nat. Commun.* **2019**, *10*, 1.